Switching between Plasmonic and Fluorescent Copper Sulfide Nanocrystals

Van Der Stam, Ward; Gudjonsdottir, Solrun; Evers, Wiel H.; Houtepen, Arjan J.

DOI
10.1021/jacs.7b07788

Publication date
2017

Document Version
Final published version

Published in
Journal of the American Chemical Society

Citation (APA)
Van Der Stam, W., Gudjonsdottir, S., Evers, W. H., & Houtepen, A. J. (2017). Switching between Plasmonic and Fluorescent Copper Sulfide Nanocrystals. *Journal of the American Chemical Society*, *139*(37), 13208-13217. https://doi.org/10.1021/jacs.7b07788

JACS
JOURNAL OF THE AMERICAN CHEMICAL SOCIETY
Article
pubs.acs.org/JACS

Switching between Plasmonic and Fluorescent Copper Sulfide Nanocrystals

Ward van der Stam,*[†] Solrun Gudjonsdottir,[†] Wiel H. Evers,[†,‡] and Arjan J. Houtepen[†]

[†]Optoelectronic Materials Section, Faculty of Applied Sciences, Delft University of Technology, van der Maasweg 9, 2629 HZ Delft, The Netherlands

[‡]Kavli Institute of Nanoscience, Delft University of Technology, van der Maasweg 9, 2629 HZ Delft, The Netherlands

Supporting Information

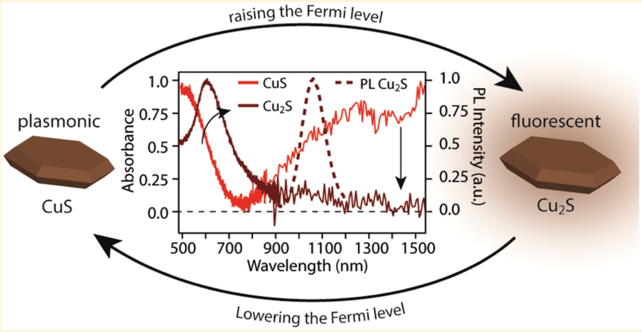

ABSTRACT: Control over the doping density in copper sulfide nanocrystals is of great importance and determines its use in optoelectronic applications such as NIR optical switches and photovoltaic devices. Here, we demonstrate that we can reversibly control the hole carrier density (varying from $>10^{22}$ cm^{-3} to intrinsic) in copper sulfide nanocrystals by electrochemical methods. We can control the type of charge injection, i.e., capacitive charging or ion intercalation, via the choice of the charge compensating cation (e.g., ammonium salts vs Li^+). Further, the type of intercalating ion determines whether the charge injection is fully reversible (for Li^+) or leads to permanent changes in doping density (for Cu^+). Using fully reversible lithium intercalation allows us to switch between thin films of covellite CuS NCs ($E_g = 2.0$ eV, hole density 10^{22} cm^{-3}, strong localized surface plasmon resonance) and low-chalcocite CuLiS NCs ($E_g = 1.2$ eV, intrinsic, no localized surface plasmon resonance), and back. Electrochemical Cu^+ ion intercalation leads to a permanent phase transition to intrinsic low-chalcocite Cu_2S nanocrystals that display air stable fluorescence, centered around 1050 nm (fwhm ∼145 meV, PLQY ca. 1.8%), which is the first observation of narrow near-infrared fluorescence for copper sulfide nanocrystals. The dynamic control over the hole doping density and fluorescence of copper sulfide nanocrystals presented in this work and the ability to switch between plasmonic and fluorescent semiconductor nanocrystals might lead to their successful implementation into photovoltaic devices, NIR optical switches and smart windows.

INTRODUCTION

Binary copper chalcogenide nanomaterials ($Cu_{2-x}E$, with E = S, Se and Te) are of interest due to their unique optoelectronic properties.[1−4] Copper sulfide ($Cu_{2-x}S$) is usually a *p*-type semiconductor with a direct band gap (E_g) that depends on its stoichiometry.[2,5−8] When the number of Cu vacancies (indicated by x in $Cu_{2-x}S$) is between 0 and 0.04, the nanocrystals attain the chalcocite and djurleite crystal structures and E_g varies from 1.1 to 1.4 eV,[3,7,9] with hole densities up to 10^{21} cm^{-3}.[6,10] When the amount of Cu is reduced, the bandgap widens (1.5 eV for $x = 0.2$, digenite crystal structure; 2.0 eV for $x = 1$, covellite crystal structure),[3,7,11] and the hole density becomes an order of magnitude higher. The easily tunable crystal structure of $Cu_{2-x}S$ nanocrystals results in a wide variety of sizes and shapes attainable for $Cu_{2-x}S$ nanocrystals by a proper choice of reaction conditions during colloidal synthesis.[12,13] Furthermore, depending on the size and shape of the $Cu_{2-x}S$ nanocrystals and the Cu to S ratio, $Cu_{2-x}S$ nanocrystals possess highly tunable localized surface plasmon resonances (LSPR) in the near-infrared (NIR) spectral region.[6,14−16] The LSPR in copper chalcogenide nanomaterials originates from excess holes in the top of the valence band,[6,15,17] which are compensated by Cu^+ deficiencies in the lattice. Besides, it has been shown that the amount of Cu^+ in $Cu_{2-x}S$ nanocrystals can be postsynthetically tailored by introducing additional Cu^+ vacancies, which increases the LSPR, or by chemically introducing Cu^+ ions, and hence, decreasing the LSPR response.[15,18]

More recently, electrochemistry has been recognized as a powerful method to tune the LSPR response of copper chalcogenide nanomaterials, and hence also the absorbance in the NIR, which is of potential interest for application in NIR switches.[19] Another, very recent, study by Lesnyak and coworkers, however, showed limited tunability of the LSPR response for covellite CuS NC films in comparison to $Cu_{2-x}Se$ NC films, ascribed to the stability of the covellite structure under the experimental conditions (CuS NC composite films in nafion, with an electrolyte solution containing tetrabutylammonium hexafluorophosphate in dichloromethane).[20] Here, we present that we can reversibly tune the hole carrier density, and hence, the LSPR response in the NIR spectral region, of covellite CuS nanocrystals by electrochemical methods, eventually switching it from a plasmonic into a fluorescent

Received: July 25, 2017
Published: August 25, 2017

DOI: 10.1021/jacs.7b07788
J. Am. Chem. Soc. 2017, 139, 13208−13217

material. By controlling the potential in an electrochemical cell we inject electrons into the CuS NCs, which shifts the band edge toward the NIR and damps the LSPR. We further show that the choice of electrolyte solution largely determines the outcome of the electrochemical charging experiments. In this way, we are able to switch between different types of doping, namely capacitive charging of CuS nanocrystals (Cs^+ and tetramethylammonium containing electrolyte solutions) and Li^+/Cu^+ ion intercalation into CuS nanocrystals. In Li^+ containing electrolyte solutions, the electrochemical charge injection is fully reversible allowing us to cycle between covellite CuS NCs (E_g = 2.0 eV, strong LSPR) and low-chalcocite CuLiS NCs (E_g = 1.2 eV, no LSPR) by reducing and oxidizing the sulfide sublattice. By calculating the number of electrons injected during our electrochemical charging experiments, we can determine the hole carrier density as a function of applied potential, and find that we can add up to 4×10^{22} electrons per cm^3. From our electrochemical experiments we also determine the diffusion coefficient of intercalating ions within copper sulfide nanocrystals ($\sim 10^{-10}$ to 10^{-11} cm^2/s). Finally, we find that when Cu^+ ions are incorporated into the covellite lattice, we permanently convert the NCs into stoichiometric low-chalcocite Cu_2S nanocrystals, with a narrow air stable photoluminescence (PL) band in the near-infrared (fwhm ~145 meV, PLQY ca. 1.8%), which is the first observation of PL in Cu_2S with a narrow PL line width. Our results show that we have dynamic control over the hole carrier density in an extremely wide doping range, allowing us to switch between metallic, plasmonic nanoparticles and semiconducting, fluorescent nanoparticles. This tunability results in the possibility to rationally design the optoelectronic properties of $Cu_{2-x}S$ nanocrystals required for the successful implementation of these nanocrystals into photovoltaic devices or applications such as NIR optical switches.

EXPERIMENTAL SECTION

Materials. Copper chloride (CuCl, 98%, Sigma-Aldrich), oleylamine (OLAM, 80%, Sigma-Aldrich), 1-octadecene (ODE, 90%, Sigma-Aldrich), sulfur powder (S, 99.99%, Alfa Aesar), octanedithiol (ODT, 98%, Sigma-Aldrich), Indium-doped Tin Oxide substrates (ITO, ~25 nm film thickness, $R_{sq} \leq 120\ \Omega/cm^2$, PGO Germany), lithium perchlorate ($LiClO_4$, 99.99%, Sigma-Aldrich), tetraoctylammonium tetrafluoroborate ($(TOA)BF_4$, >98%, Sigma-Aldrich), tetrabutylammonium perchlorate ($(TBA)ClO_4$, >98%, Sigma-Aldrich), tetramethylammonium hexafluorophosphate ($(TMA)PF_6$, >98%, Sigma-Aldrich), cesium perchlorate ($CsClO_4$, 99.995%, Sigma-Aldrich), copper(I) tetrafluoroborate ($CuBF_4$, >98%, Sigma-Aldrich), ferrocene (Fc, 98%, Sigma-Aldrich). Anhydrous solvents (methanol, 99.8%, butanol, 99.8%, toluene, 99.8%, tetrachloroethylene (TCE, >99%) and acetonitrile, 99.99%) were all purchased from Sigma-Aldrich. Acetonitrile was dried before use in an Innovative Technology PureSolv Micro column. All other chemicals were used as received.

Synthesis of CuS Nanocrystals. The CuS nanocrystals were synthesized according to the method described by Xie et al.[18] A sulfur precursor solution was prepared by degassing a mixture containing 0.032 g (1 mmol) of sulfur powder, 5 mL of OLAM, and 5 mL of ODE in a 50 mL three-neck flask at 130 °C under vacuum for 30 min. Subsequently, the flask was cooled to room temperature under N_2 atmosphere. After, 0.050 g (0.5 mmol) of CuCl powder was added to the sulfur solution, and the flask was pumped to vacuum at room temperature for 1 h. Subsequently, the solution was heated to 200 °C under N_2 flow and the solution was kept at the reaction temperature of 200 °C for an additional 30 min. The resulting dark green solution was cooled to room temperature and the NCs were precipitated three times with a 1:1:1 volume mixture of crude solution:methanol:butanol in a nitrogen filled glovebox. Afterward, the NCs were centrifuged at 3000 rpm and the clear supernatant was decanted. Finally, the NCs were redispersed in toluene and/or tetrachloroethylene.

CuS Thin Film Preparation. Nanocrystal films were prepared by dipcoating an ITO substrate in a concentrated colloidal dispersion of CuS NCs in TCE. The NCs were cross-linked with octanedithiol (ODT), and the NC films were washed with methanol to remove excess cross-linking ligands. The ITO substrates were held in the three solutions for 30 s, and allowed to dry for an additional 30 s between dipping steps. A KSV NIMA dip coater was used. This cycle was repeated 10 times, in order to obtain a sufficiently thick NC film (~1 μm).

(Spectro)electrochemistry. (Spectro)electrochemical measurements were performed according to the procedure described previously, except that all experiments were performed inside a N_2 glovebox with acetonitrile that was dried with an Innovative Technology PureSolv Micro column.[21] The CuS NC films were immersed in a 0.1 M $LiClO_4$ electrolyte solution in acetonitrile, together with a Ag wire pseudoreference electrode and a Pt sheet counter electrode. The supporting electrolyte was 0.1 M cation-perchlorate, cation-hexafluorophosphate or cation-tetrafluoroborate electrolyte solutions (cation = TOA, TBA, TMA, Cs, Cu). The potential of the NC film on ITO was controlled with a PGSTAT128N Autolab potentiostat. Changes in the absorption of the NC film as a function of applied potential were recorded simultaneously with a fiber based UV−VIS spectrometer (USB2000, Ocean Optics) and a NIR spectrometer (NIRQuest 256, Ocean Optics), with a combined range of about 300 to 2500 nm. For all films, the cyclic voltammograms (CVs) were recorded starting from open circuit potential (~ −0.2 V vs Ag for CuS-ITO), scanning at different rates of 20 mV/s to 1.0 V/s. Every CV scan was repeated five times. Unless stated otherwise, all potentials are given with respect to a Ag wire pseudoreference electrode immersed in the electrolyte solution. Its potential (−4.77 eV vs vacuum) was calibrated with a ferrocene/ferrocenium couple (Figure S1).[22]

Optical Spectroscopy. Samples for optical measurements in solution were prepared by diluting the stock solution of washed NCs with anhydrous TCE under nitrogen. Samples were stored in closed quartz cuvettes. Absorption and photoluminescence (PL) measurements were also conducted directly on the CuS-ITO electrode described above. Absorption spectra were measured on a double-beam PerkinElmer Lambda 1050 UV/vis spectrometer. Photoluminescence spectra were recorded on an Edinburgh Instruments FLS980 spectrofluorimeter equipped with a 450 W xenon lamp as excitation source and double grating monochromators.

PL Quantum Yield (PLQY). Measurements were performed on the same spectrofluorimeter mentioned above. A PbS NC colloidal dispersion was prepared as reference NC solution (OD ~ 0.2 at 800 nm, just as the Cu_2S NC film) and the PLQY was measured directly in an integrating sphere and established to be 71%. The PL of the Cu_2S NC film and PbS NC dispersion were then measured with the same excitation and emission slits and the PL intensities were directly compared in order to get an estimate for the PLQY. We note that the obtained PLQY in this way represents a rough estimate, since we do not correct for the direction of the PL from a NC film.

X-ray Diffractometry (XRD). XRD measurements were performed with a Bruker D8 DISCOVER, equipped with a Cu K-alpha X-ray source (λ = 1.5418 Å), under grazing incidence conditions (angle of incidence 1°), to minimize the contribution from the ITO substrate. The CuS-ITO electrode described above was directly used for the XRD measurements.

Raman Spectroscopy. Raman spectra were recorded on a Renishaw InVia Raman spectrophotometer, equipped with an optical microscope, operating at 50× magnification. The sample was excited with a 785 nm laser for 60 s. The spectrophotometer has a spectral resolution of <0.5 cm^{-1}. The CuS-ITO electrode described above was used for the Raman measurements.

Transmission Electron Microscopy (TEM). TEM images were acquired using a JEOL JEM-1400plus TEM microscope operating at 120 kV. Samples for TEM imaging were prepared by dropcasting a toluene solution of NCs onto a carbon-coated copper (400-mesh) TEM grid.

X-ray Photoelectron Spectroscopy (XPS). Measurements were performed on a Thermo Fisher K-Alpha spectrometer, equipped with an Al K*α* source (1486 keV). Wide survey scans were acquired at a pass energy of 160 eV. High-resolution scans were performed at a pass energy of 10 eV, with 0.05 eV steps. The scans were typically repeated 50 times in order to improve the signal-to-noise ratio. The pressure in the analysis chamber was maintained below 2×10^{-7} mbar for data acquisition. The binding energy scale was referenced with respect to the C 1s peak (284.8 eV). The above-mentioned CuS-ITO electrode was used for XPS measurements.

Thickness Determination. A Dektak profilometer was used to determine the film thickness. A cantilever force of 3 mg was used and scans were acquired for 5 min over a total distance of 1.5 cm.

RESULTS AND DISCUSSION

Synthesis of CuS NC Thin Films with NIR LSPR. Hexagonal nanoplatelets (NPLs) are observed with TEM (Figure 1a), with lateral sizes ranging from 500 nm to 1 *μ*m and a thickness of ∼10 nm. The crystal structure was analyzed by performing Electron Diffraction (ED) (inset Figure 1a) and X-ray Diffraction (XRD) measurements (Figure S2, Supporting Information), which confirms the covellite CuS crystal structure. Absorption measurements reveal strong absorption in the visible (bandgap absorption) and NIR part (localized surface plasmon resonance, LSPR) of the electromagnetic spectrum (Figure 1b). As can be seen in Figure 1b, the absorption spectrum for CuS NCs dispersed in TCE is different than for thin films of ∼1 *μ*m thickness. This can be explained by the different dielectric medium surrounding the CuS NCs (TCE for the colloidal dispersion, air for the NC films).[6] The broad LSPR feature observed for our CuS NC films (Figure 1b) originates from the broad lateral size dispersion.[23]

Covellite (CuS) represents a special case within the copper sulfide crystal structure family in terms of its electronic properties. In covellite CuS, the crystal structure is build up from trilayers of Cu and S atoms, and each trilayer is bound perpendicularly to other trilayers by covalent S−S bonds (Figure 1c).[17,18] The electronic structure of covellite has been debated extensively.[17,24,25] It has been suggested that the structure should be viewed as $(\mathrm{Cu}^{+})_3\mathrm{S}^{2-}(\mathrm{S}_2)^{-}$, indicating that the disulfide unit has a net charge of −1, corresponding to a hole in antibonding orbitals of the disulfide bonds, which form the top of the valence band.[25−27] Therefore, covellite is a degenerately *p*-doped semiconductor (with strong NIR LSPR, see Figure 1b), with one hole per $\mathrm{Cu_3S_3}$ unit, corresponding to a theoretical hole density of 9.7×10^{21} cm^{-3} (see Supporting Information, Supporting Methods 1 for calculation). In reality, this number may vary since more electrons can be added or removed from these disulfide antibonding orbitals. That is, the hole density depends on the Fermi level of the environment, as shown very clearly by the electrochemical measurements below.

Tuning the Hole Carrier Density in Copper Chalcogenide Nanomaterials. Although the presence of holes in the top of the valence band results in very interesting LSPR bands in the NIR, it also quenches the radiative recombination in $\mathrm{Cu}_{2-x}\mathrm{S}$ nanocrystals, due to the high carrier density of background holes, which likely results in efficient nonradiative Auger recombination. Previous reports on low-chalcocite nanocrystals show that the stoichiometry of the synthesized $\mathrm{Cu_2S}$ nanocrystals is close to 2:1, but nevertheless the NCs do not display PL features, despite the direct bandgap of $\mathrm{Cu_2S}$.[6,8] Kriegel et al. have reported weak photoluminescence for stoichiometric $\mathrm{Cu_2S}$ NCs treated with excess copper ions, where the PL band was characterized by short PL lifetimes (which is the sum of radiative and nonradiative recombination) and a broad PL line width.[16] Possibly, the short PL lifetime is due to the presence of a small amount of background holes, which results in efficient Auger recombination.

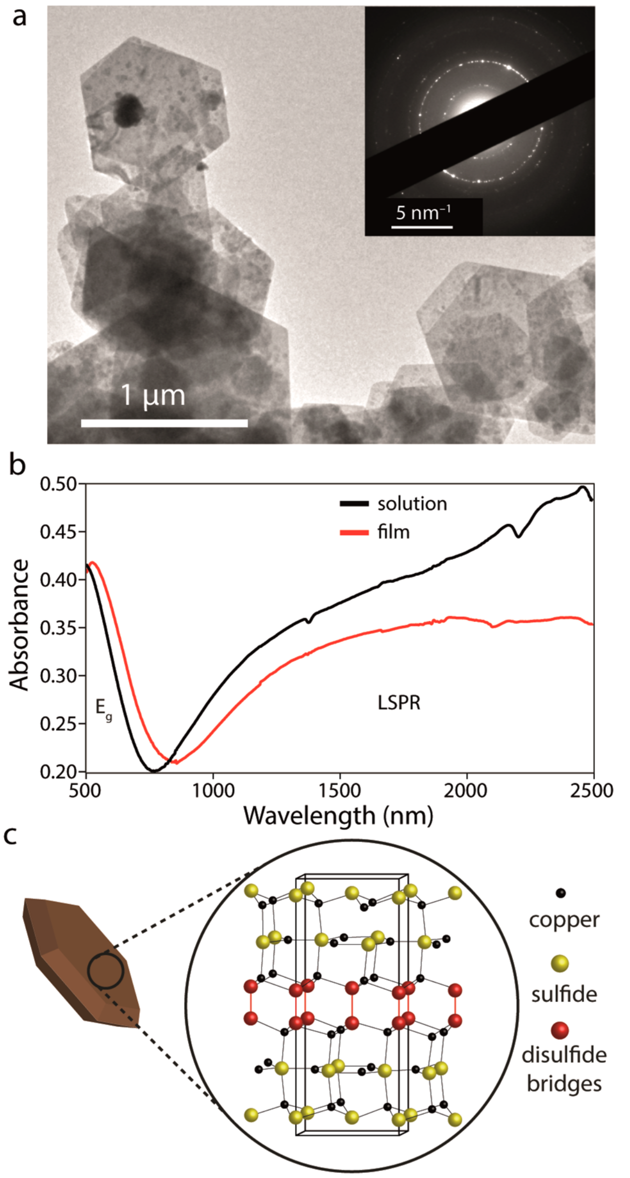

Figure 1. Structural and optical characterization of CuS nanocrystals. (a) Transmission Electron Microscopy (TEM) image and (inset) 2D Electron Diffraction (ED) pattern of CuS NCs. (b) Absorption spectra of CuS NCs in solution (black line; solvent TCE) and of a CuS NCs film (red line). (c) Schematic representation of a CuS nanocrystal and the covellite CuS crystal structure, clearly displaying the disulfide bridges (red spheres).

The preparation of stoichiometric $\mathrm{Cu_2S}$ without residual holes might be beneficial for PV cells.[28,29] In fact, $\mathrm{Cu_2S}$ was one of the first materials to be considered as PV absorber material, due to its bulk bandgap (1.1 eV) and high absorption coefficient (10^4 cm^{-1}), but *p*-type doping due to the presence of holes has hampered their implementation into PV devices.[2,30,31] It is thus evident that control over the doping density in copper sulfide nanocrystals is of crucial importance for their optoelectronic properties, and hence, their potential

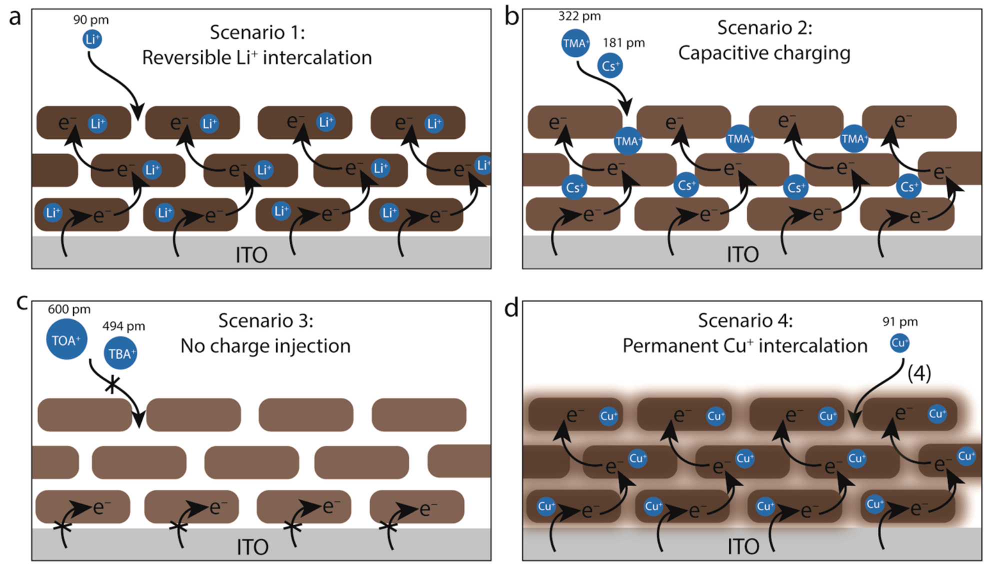

Figure 2. Schematic representation of the four regimes of electrochemical charging of CuS NCs. (a) Li^+ ions intercalate into the NCs upon electrochemical charging in Li^+ containing electrolyte solutions, converting CuS NCs into CuLiS NCs. (b) Charging in the presence of TMA^+ and Cs^+ lead to partial capacitive charging of the NC films, since TMA^+ and Cs^+ are too large to penetrate into the CuS NCs. (c) TOA^+ and TBA^+ are too large to penetrate into the voids and therefore no charge injection into CuS is possible. (d) Cu^+ gets incorporated into the NCs upon reduction of the anion sublattice, resulting in permanent conversion of CuS NCs into Cu_2S NCs which display air stable NIR photoluminescence.

for implementation into optoelectronic devices. Therefore, we present a strategy for tuning the charge injection and hole carrier density in covellite CuS nanocrystals, which eventually results in intrinsic Cu_2S nanocrystals. We chose a spectroelectrochemical approach, in which we control the concentration of charge carriers electrochemically, while monitoring the temporal evolution of the NC film absorbance.[21,32] We use an electrochemical cell with a three electrode configuration: a working electrode (WE), counter electrode (CE) and pseudoreference electrode (PRE). The WE was prepared by dipcoating CuS NCs on indium-doped tin oxide (ITO) substrates and cross-linking the CuS NCs with octanedithiol (ODT) ligands in order to enhance the mechanical stability and electron transport throughout the film, as described in more detail in the Experimental Section. The complete electrochemical cell consisted of a quartz cuvette, the above-mentioned ITO-CuS working electrode (WE), the counter electrode (CE, Pt plate), a pseudoreference electrode (PRE, Ag wire) and an electrolyte solution (typically 0.1 M $LiClO_4$ in acetonitrile), as reported by us previously (Figure S3).[21]

Model with Four Scenarios for Electrochemical Charging and Ion Intercalation. As tentatively calculated in the Supporting Information, the hole density in covellite is $\sim 10^{22}$ cm^{-3} and its elimination requires the addition of a high density of electrons. This is only possible if sufficient charge compensation is available. In electrochemical charging experiments such charge compensation comes from cations in the electrolyte solution, which diffuse into the film of NCs to screen the electron charge. In a previous report, we have shown that the electrochemical charging of CdSe NCs strongly depends on the void size and the size of the counterion in solution.[21] Here, we investigated electrochemical charging of CuS NC films in different electrolyte solutions and we distinguish the following four regimes, schematically depicted in Figure 2. (1) Li^+ ions are used in the electrolyte solution as charge compensating ions. The Li^+ ions are small enough (ionic radius r^+ of 90 pm) to intercalate the covellite crystal lattice and occupy the Cu sites present in the CuS NCs (Figure 2a). (2) The counterions are small enough to penetrate into the NC film and occupy the voids between the NCs, but cannot be incorporated into the NCs, since they are much larger than Cu^+ and therefore not expected to fit in the CuS lattice (TMA^+ and Cs^+, r^+ between 0.18 and 0.32 nm), resulting in capacitive charging of the NC film (Figure 2b). Here, capacitive charging is defined as charging due to the formation of an electrical double layer, in this case on the surface of each NC. (3) Electrochemical charging is not possible if the counterions are too large to occupy the voids between the NCs (TOA^+ and TBA^+, $r^+ > 0.4$ nm, Figure 2c). (4) Cu^+ ions are present in solution, which get incorporated into the CuS lattice upon reduction of the anion sublattice and cannot be removed by applying positive potentials vs Ag pseudoreference (Figure 2d), resulting in intrinsic Cu_2S NCs. In the rest of this paper, we will discuss these four regimes in more detail, starting with Scenario 1: Reversible Li^+ intercalation.

Scenario 1: Electrochemical Charging of CuS NC Films in Li^+ Electrolytes. We first explore electrochemical charging of CuS NC films in Li^+ containing electrolyte solutions. Li^+ electrolyte solutions are commonly used in electrochemical charging experiments due to the small ionic radius (90 pm) and high diffusivity of Li^+ ions in solution, which ensures rapid charge compensation upon variations of the Fermi level. When a sufficiently large potential difference is applied between the PRE and WE, electrons flow into the CuS NCs, thereby raising the Fermi level of the semiconductor. At the same time, positive ions (Li^+ in this case) flow into the porous NC film to ensure charge neutrality. The cyclic voltammogram (CV) in Figure 3a shows that electrons are injected into the CuS NCs around −0.8 V vs Ag PRE (∼ −4.0 V vs vacuum), with maximum current density at −1.0 V (∼ −3.8 V vs vacuum). When the scan is reversed, electrons are taken out of the WE around −1.0 V and the current density reaches a maximum around −0.8 V.

DOI: 10.1021/jacs.7b07788
J. Am. Chem. Soc. 2017, 139, 13208−13217

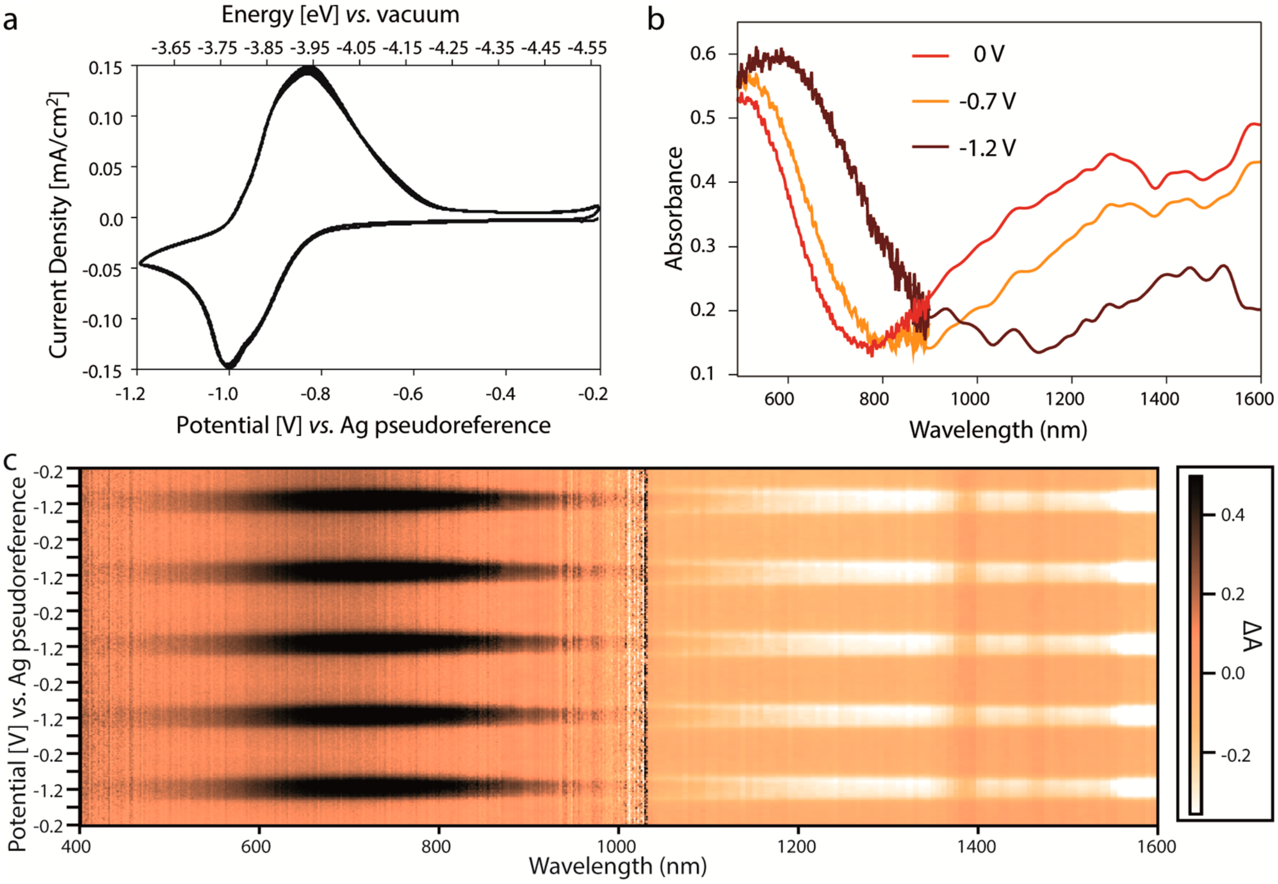

Figure 3. Spectroelectrochemical measurements on CuS nanocrystals films. (a) Cyclic voltammograms of electrochemical charging of a CuS NC film in 0.1 M $LiClO_4$ in acetonitrile (5 cycles, scan rate 0.1 V/s). (b) Absorbance at different applied potentials, showing the small shift and bleach of the bandgap and LSPR absorbance when −0.7 V is applied (orange line), and maximum shift and bleach when −1.2 V is applied (brown line). Absorbance of parent CuS NC film is also displayed (red line). (c) Differential absorbance as a function of the applied potential in the visible part and near-infrared (NIR) part of the electromagnetic spectrum, showing strong induced absorption near the band edge between 600 and 900 nm and a bleach of the NIR LSPR between 1100 and 1600 nm when −1.2 V vs Ag PRE is applied.

While changing the potential in a linear sweep experiment, the absorption spectrum changes considerably. Figure 3b displays the absorbance at three different applied potentials (0, −0.7 and −1.2 V vs Ag PRE) and Figure 3c shows the differential absorbance plots as a function of the applied potential with respect to the Ag PRE. It can be seen that the bandgap absorbance and LSPR slightly redshift at −0.7 V (Figure 3b). When a potential of −1.2 V is applied, induced absorption between 600 and 900 nm and a bleach of the LSPR band in the NIR are observed (Figure 3b,c). This indicates that absorption associated with the bandgap shifts to higher wavelengths, i.e., the bandgap decreases. At the same time, the NIR LSPR, associated with excess holes in the valence band of CuS, is damped as more electrons are injected and the excess holes are annihilated, indicating that the hole carrier density decreases. These observed optical transitions bear similarities with the optical transitions for the chemical transformation of covellite CuS to low-chalcocite Cu_2S.[18] In that case, additional Cu^+ ions are introduced in the form of tetrakisacetonitrile copper(I) hexafluorophosphate, which damps the LSPR and shifts the bandgap to longer wavelengths. The authors showed with XPS measurements that the sulfur sublattice is initially in the −1 oxidation state, consisting of a mixture of covalent S−S bonds and sulfide anions, which is reduced to the −2 oxidation state. The electrons required for the reduction of the covalent S−S bonds are provided by a subsequent oxidation of a portion of the Cu^+ ions in solution to Cu^{2+}.[18] We propose a similar reduction reaction of the anion sublattice in covellite, which induces the transformation into low-chalcocite. In this case, the electrons necessary for this transformation are supplied electrochemically.

When using Li^+ containing electrolytes, the covellite to low-chalcocite transformation is fully reversible, and can be cycled many times (Figure 3c). In the CV scans a small charging current is observed between −0.2 and −0.8 V, corresponding to a change in the hole carrier density of $\sim 4.0 \times 10^{21}$ cm^{-3} at −0.8 V (see Supporting Information Figure S4). We note that this calculated density is ∼40% of the calculated density of holes in covellite CuS, assuming one hole per Cu_3S_3 unit (see calculations in Supporting Information, Supporting Methods 1). No clear features are observed in the CV wave in this potential range, indicating that possible contributions of spurious side reactions like reducible defects,[33] has a negligible effect on the experimentally determined hole carrier densities. Therefore, we attribute this current and the corresponding optical changes to capacitive charging of the NC film with Li^+ ions likely occupying void space between the NCs but not introducing a phase transition of the crystal lattice.

When the reduction potential for the anion sublattice is reached (−1.0 V vs Ag PRE), a much larger current density is

DOI: 10.1021/jacs.7b07788
J. Am. Chem. Soc. 2017, 139, 13208−13217

observed, which we attribute to the reduction of the disulfide bridges in the covellite crystal structure (number of injected electrons: 4.0×10^{22} cm^{-3}, see Supporting Information Figure S4). For these hole carrier density calculations, we assume a one-to-one relationship between the number of injected electrons and the hole carrier density, since we do not observe side reactions like reducible defects,[33] as mentioned above. The reduction of the disulfide bridges corresponds to complete filling of their antibonding orbitals making the bonds unstable and causing a change in the overall crystal structure, as shown below.

Likely, Li^+ intercalates into the CuS lattice to compensate the injected electrons, following the electrochemical half reaction

$$\mathrm{CuS} + \mathrm{Li}^+ + \mathrm{e}^- \rightleftarrows \mathrm{CuLiS}$$

in which the equilibrium is shifted to the product CuLiS by supplying an excess of electrons. Li^+ intercalation is commonly observed in electrochemical experiments,[34−36] due to the small ionic radius of Li^+ (r^+ is 90 pm), often resulting in phase transformations, for example from tetragonal anatase TiO_2 into orthorhombic $Li_{0.5}TiO_2$.[37] Electrochemical intercalation of Li^+ into bulk CuS electrodes has also been observed, resulting in Li_xCuS crystal phases.[38,39] Since the ionic radius of Li^+ and Cu^+ are the same (90 and 91 pm, respectively), Li^+ can easily occupy Cu sites. However, the Cu_2S and LiCuS lattices are indistinguishable by XRD measurements, due to the similar ionic radius of Li^+ and Cu^+.[38,39] We therefore propose that Li^+ intercalates into the CuS NCs to ensure charge neutrality after reduction, forming a metastable low-chalcocite CuLiS crystal phase, which can be converted back to CuS by reversing the potential scan direction.

Diffusion Coefficient of Intercalating Li^+ Ions in $Cu_{2-x}S$. To investigate the charge compensation by Li^+ further, cyclic voltammograms were recorded at different scan rates for electrolyte solutions with varying concentrations of $LiClO_4$ in acetonitrile (Figure 4 and Figure S5−6). As can be seen in the insets in Figure 4, the maximum peak current (I_p) scales linearly with the square root of the scan rate for all electrolyte concentrations. This is typical for diffusion-limited electrochemical reactions at planar electrodes, where the current is set by the rate of diffusion of the reacting species to the electrode surface. The current situation is slightly different as in this case ions diffuse through a porous solid, but we propose that a similar description holds, as was shown for other porous material electrodes.[40,41] From the slope of a linear fit to I_p vs $v^{1/2}$, the diffusion coefficient can be determined according to the Randles−Sevcik equation,[42]

$$I_p = 2.69 \times 10^5 n^{3/2} A D^{1/2} C v^{1/2} \tag{1}$$

with n the number of electrons, A the electrode area (2.0 cm^2), C the concentration of the diffusing species (Li^+, 0.1M), D the diffusion coefficient (in cm^2/s) and v the scan rate (in V/s). From the peak separation at very low scan rates (ΔE_p = 56 mV), the number of electrons n was determined to be 1, since $\Delta E_p = 59$ mV/n. This observed reduction is thus a one electron process, in agreement with the overall reduction of the anionic sublattice from −1 oxidation state to −2. We find diffusion coefficients in the order of 10^{-10} to 10^{-11} cm^2/s. Furthermore, we find that the diffusion coefficient decreases almost 2 orders of magnitude by increasing the electrolyte concentration from 0.1 to 1.0 M $LiClO_4$ in acetonitrile, from 9.84×10^{-10} cm^2/s (Figure 4a) to 1.39×10^{-11} cm^2/s (Figure 4c), potentially due to jamming in the porous NC film at higher salt concentrations.

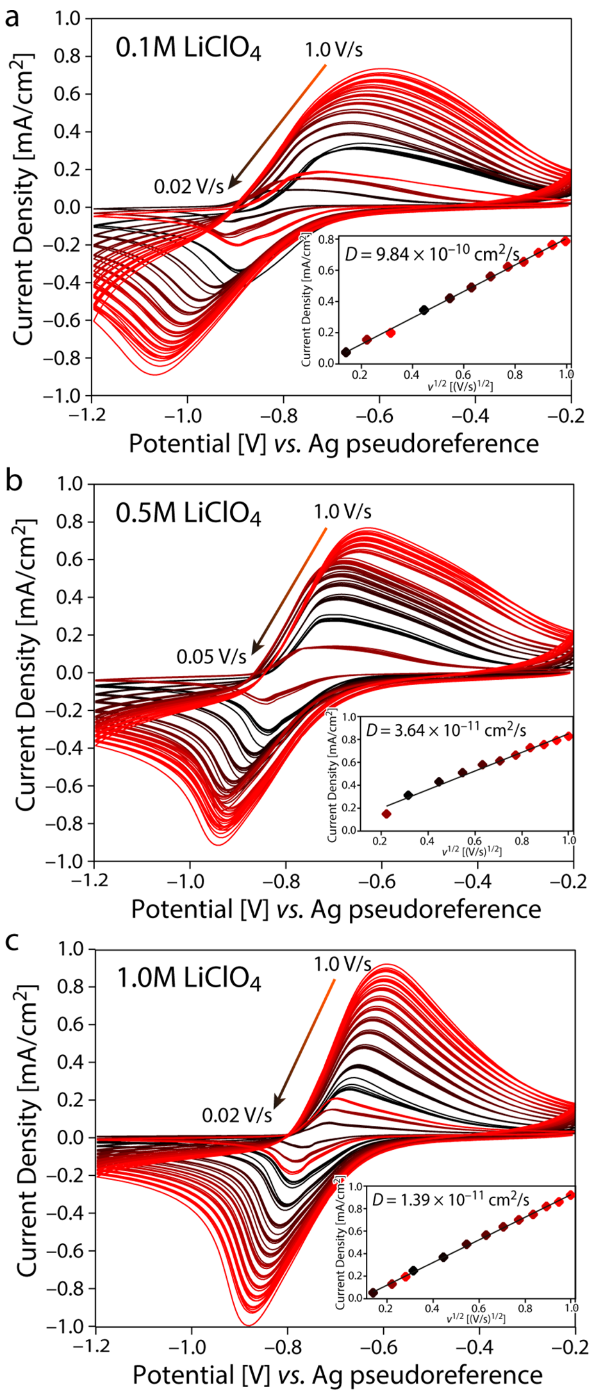

Figure 4. Randles−Sevcik plots for different electrolyte concentrations. (a) Cyclic voltammograms at different scan rates for a 0.1 M $LiClO_4$ in acetonitrile electrolyte, (b) a 0.5 M $LiClO_4$ in acetonitrile electrolyte and (c) a 1.0 M $LiClO_4$ in acetonitrile electrolyte solution. The cyclic voltammograms show a linear dependence between peak current and square root of the scan rate (insets). From the slope of the linear fit, the diffusion coefficient is determined. Diffusion coefficients in the order of 10^{-10} and 10^{-11} cm^2/s are found, corresponding to Li^+ diffusion in the covellite CuS lattice (insets).

These experimentally determined diffusion coefficients are too small to account for Li^+ diffusion in solution (typical values around 10^{-5} cm^2/s).[35] Rather, they are in good agreement with reported values for Cu^+ ion diffusion (r^+ Cu^+ 91 pm, r^+ Li^+ 90 pm) in bulk $Cu_{2-x}S$ (~10^{-10} cm^2/s).[43,44] Furthermore, the experimentally determined diffusion coefficients are also ~2 orders of magnitude smaller than diffusion coefficients of ions in porous electrodes (typical values around 10^{-8} cm^2/s).[40,41] Therefore, we state that the observed diffusion coefficients can be ascribed to Li^+ ion diffusion within the CuS NC lattice, which is the rate-limiting step in the reduction of covellite into low-chalcocite.

Scenario 2 and 3: Electrochemical Charging in Electrolyte Solution Containing Larger Counterions. To test our hypothesis that Li^+ is indeed intercalated in the CuS lattice, we studied electron injection into CuS nanoplatelets in 0.1 M electrolytes with different sizes of positive counterions (TOA^+, TBA^+, TMA^+, Cs^+). Due to the large ionic radii of these cations, they are not expected to intercalate into the CuS NCs. All measurements were conducted on the same NC film, starting with the largest ion (TOA^+). We find that charge injection is only possible if a sufficiently small counterion is present in the electrolyte, similar to what was observed previously for CdSe NC films.[21] No efficient charge injection is observed in the same potential window (−0.2 V to −1.2 V vs Ag PRE) when TOA^+ and TBA^+ are used ($r^+ > 0.6$ and 0.494 nm, respectively, Supporting Information Figure S7a). When TMA^+ is employed in the electrochemical charging experiments, small differential absorbance changes are observed (Supporting Information, Figure S8), suggesting that TMA^+ is sufficiently small ($r^+ = 0.322$ nm) to charge part of the NPLs film, but is insufficient for full conversion of the CuS NPLs film into Cu_2S NPLs. The same holds for Cs^+ ($r^+ = 0.181$ nm, Supporting Information Figure S9). The ionic radii of TMA^+ and Cs^+ are much larger than that of Cu^+ (91 pm) and therefore TMA^+ and Cs^+ are not expected to fit in the Cu vacancies. We conclude that the observed optical changes are due to capacitive charging of the CuS NCs and the injected charges are balanced externally by TMA^+ and Cs^+ ions. Finally, the NC film was charged in the presence of Li^+ ions and the same reduction and oxidation waves are observed as shown previously (see Figure 3 and Figure S10). These results are summarized in Table 1, which shows that the current density at an applied potential of −1.0 V vs Ag PRE scales with the size of the charge compensating ion.

Table 1. Summary of Spectroelectrochemical Measurements on CuS Nanocrystal Films in Different Supporting Electrolyte Solutions, Containing Positively Charged Counterions with Varying Ionic Radius

counterion	ionic radius (nm)	current density at −1.0 V ($\mu A/cm^2$)	ΔA LSPR at 1200 nm (mOD)
TOA^+	>0.6	–	–
TBA^+	0.494	2.5	–
TMA^+	0.322	22	~ −22
Cs^+	0.181	105	~ −30
Li^+	0.090	1150	~ −60

Scenario 4: Intercalation of Cu^+ Ions and Phase Transformation from Covellite to Low-Chalcocite. If we change the electrolyte solution to 0.1 M $CuBF_4$ in acetonitrile, similar charging currents (~1 mA/cm^2) and optical changes are observed as for Li^+ containing electrolyte solutions, except that the changes are irreversible in the same potential window (−0.2 to −1.2 V vs Ag PRE, see Figure S11 for the cyclic voltammogram), indicating that we permanently convert the covellite CuS NCs into low-chalcocite Cu_2S NCs. The optical features are discussed in more detail below. The permanent changes can be explained by intercalation of Cu^+ ions in the CuS lattice as a result of the reduction of the anion sublattice, following the electrochemical half reaction

$$CuS + Cu^+ + e^- \rightleftarrows Cu_2S$$

This equilibrium is strongly in favor of the product Cu_2S in the presence of a large amount of electrons, as is the case here in our electrochemical approach. In the CuS crystal structure, the anions are on an hcp sublattice, with covalent bonds between sulfur layers (Figure 5a).[2,14,17,45] In the low-chalcocite Cu_2S phase, the anions are also on an hcp sublattice, meaning that these crystal structures are compatible with each other (Figure 5b).[46−48] However, in order to accommodate the

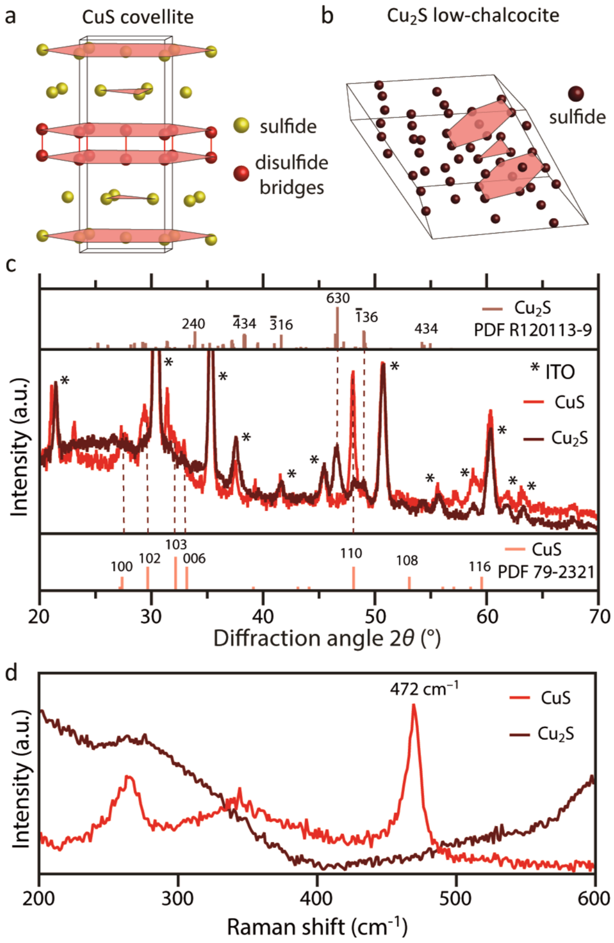

Figure 5. Phase transformation of covellite CuS into low-chalcocite Cu_2S. (a) Model showing the covalent S–S bond and hcp anion sublattice in covellite CuS. (b) Model showing hcp anion sublattice of low-chalcocite Cu_2S. (c) XRD measurements of CuS NCs before (red line) and after (brown line) electrochemical charging in the presence of Cu^+ ions. The XRD pattern of the CuS NCs shows the characteristic (110) reflection for covellite, whereas the XRD pattern after electrochemical charging clearly shows the (630) reflection of low-chalcocite Cu_2S. Reference bars are from PDF cards 79−2321 and R120113−9 for covellite CuS and low-chalcocite Cu_2S, respectively. (d) Raman spectrum for a film of CuS NCs (red line), showing the characteristic S–S stretching mode at 472 cm^{-1}, and Raman spectrum for a film of Cu_2S NCs (brown line), in which no disulfide bridges are observed at 472 cm^{-1}, indicating successful reduction of the anionic sublattice.

electrochemically injected electrons and intercalated Li^+ or Cu^+ ions, the lattice has to rearrange considerably. When Li^+ ions are intercalated, the low-chalcocite crystal structure is metastable and can easily be oxidized back to covellite CuS, evidenced by the reversible electrochemical and optical features (see Figure 3). However, when Cu^+ ions are intercalated, the low-chalcocite phase is stabilized and the Cu^+ ions can not be extracted from the lattice in the same potential window. Subsequent ex situ X-ray Diffractometry and Raman spectroscopy measurements corroborate the phase transformation of CuS NCs into Cu_2S NCs upon Cu^+ intercalation, since the characteristic covellite Raman peaks and XRD reflections have disappeared (Figure 5c,d) and low-chalcocite reflections are observed. The XRD pattern of the CuS NPLs shows the characteristic (110) reflection around $2\theta = 48°$ (red line in Figure 5c), which disappears when a sufficiently large potential is applied (brown line in Figure 5c). Sharp reflections at 46° and 48° are observed after Cu^+ intercalation, corresponding to the (630) and (−136) lattice planes of low-chalcocite Cu_2S. The phase transformation was further corroborated with ex situ Raman measurements (Figure 5d). The characteristic Raman features for covellite CuS were observed before electrochemical charging (sharp peak at 472 cm^{-1}, associated with the S−S stretching mode),[18] while these features are no longer observed after electrochemical charging (see Figure 5d and Figure S12, Supporting Information), which provides direct evidence for cleavage of these disulfide bonds upon reduction. XPS measurements further confirm the reduction of the anionic sublattice to a −2 oxidation state, since the characteristic three S 2p peaks for the disulfide bonds are not observed after Cu^+ intercalation (Figure S13).[18]

Optical Properties after Cu^+ Intercalation. When Cu^+ ions get intercalated, the same absorbance is observed as for the intercalation of Li^+ ions in CuS nanocrystals. In this case, however, the optical changes are permanent and cannot be reversed when the scan direction is reversed (Figure 6a). This indicates that we can reduce covellite CuS to low-chalcocite Cu_2S, but cannot oxidize it back in the same potential window when Cu^+ ions are incorporated. Interestingly, it is found that the final low-chalcocite Cu_2S NCs display photoluminescence centered around 1050 nm (Figure 6b, dashed brown line) with a PLQY of approximately 1.8% (see Experimental Section for details) which is stable in air for at least 2 months. As discussed above, photoluminescence is typically not encountered in Cu_2S nanocrystals, due to exciton annihilation via Auger recombination. Several reports have shown that Cu_2S is highly prone to oxidation toward the Cu deficient djurleite $Cu_{1.96}S$ phase under ambient conditions, due to the high thermodynamic stability of the djurleite phase owing to its lower crystallographic symmetry compared to chalcocite Cu_2S.[27,30,49,50] Furthermore, it was shown that Cu_2S NCs without Cu defects were nearly impossible to synthesize or even store for a long period of time.[51] Our results show that fully stoichiometric stable Cu_2S nanocrystals can be obtained by electrochemical methods, resulting in narrow PL in the NIR (fwhm of ∼145 meV), which is the first example of air stable fluorescent Cu_2S NCs.

The possibility to tune the carrier density (and hence the NIR LSPR response) of CuS NC films on demand by reversibly intercalating and removing Li^+ ions into and from the covellite CuS lattice, and subsequently convert the film into fully stoichiometric Cu_2S NC films with NIR PL by permanent incorporation of Cu^+, provides a unique set of tools to design NC films for optoelectronic applications. For example, tunable and switchable visible and NIR transmission is of interest for application in smart windows, used for heat-dissipation and -management of buildings.[52−54] Furthermore, the preparation of stoichiometric Cu_2S without residual holes might be beneficial for PV cells.[28,29]

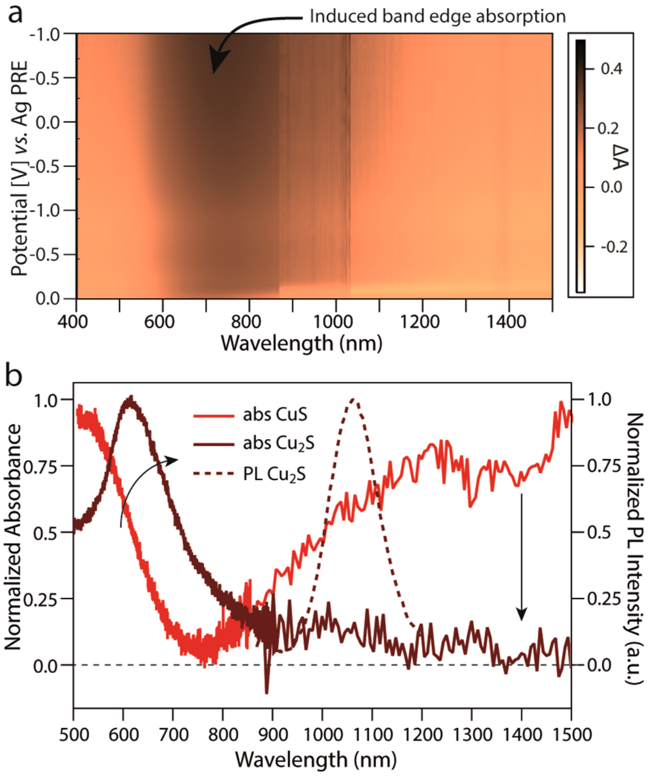

Figure 6. (a) Differential absorbance as a function of applied potential of a CuS NC film upon Cu^+ intercalation in a 0.1 M $CuBF_4$ in acetonitrile electrolyte solution. The optical changes cannot be reversed when the potential scan direction is reversed. (b) Absorption (brown full line) and photoluminescence (dashed brown line) spectra of Cu_2S NCs films obtained after Cu^+ intercalation. The PLQY of the Cu_2S NC film was established to be ca. 1.8%. Absorbance of the parent CuS NC film is also displayed (red full line).

CONCLUSIONS

We have shown that we have dynamic control over the hole carrier density in copper chalcogenide nanocrystals by electrochemically injecting electrons, tuning it from degenerately doped *p*-type plasmonic materials to intrinsic fluorescent nanocrystals. By the choice of the charge-compensating ion in solution, we can for example switch between covellite CuS nanocrystals and low-chalcocite CuLiS nanocrystals by Li^+ intercalation (diffusion coefficient 10^{-11} cm^2/s), thereby tuning the absorbance in the near-infrared due to damping of the LSPR. We can also permanently convert covellite CuS into low-chalcocite Cu_2S, by supplying Cu^+ ions in the electrolyte solution while raising the Fermi level. In this way, the Cu^+ ions get incorporated and subsequently stabilize the low-chalcocite Cu_2S crystal structure. Interestingly, we find that the Cu_2S nanocrystals obtained by electrochemically introducing Cu^+ ions display air stable photoluminescence in the near-infrared with a narrow photoluminescence bandwidth (fwhm ∼145 meV, PLQY ca. 1.8%), which has not been observed before for copper chalcogenide nanocrystals. Precise control over the doping density in copper chalcogenide nanomaterials by capacitive charging and/or ion intercalation and the possibility to bestow the nanocrystals with novel functionalities might impact on their implementation into applications in the field of smart windows, near-infrared optical switches, Li-ion batteries and photovoltaic cells.

■ ASSOCIATED CONTENT

Supporting Information

The Supporting Information is available free of charge on the ACS Publications website at DOI: 10.1021/jacs.7b07788.

> Cyclic voltammograms of ferrocene, XRD pattern of ITO substrate, calculation of the theoretical charge carrier density, schematic representation of the electrochemical cell, differential absorbance plots for cyclic voltammograms in higher concentration electrolyte solutions, cyclic voltammograms and differential absorbance plots for different sizes of positive counterion electrolyte solutions, cyclic voltammograms in Cu^+ electrolyte solutions, XPS measurements (PDF)

■ AUTHOR INFORMATION

Corresponding Author

*w.vanderstam@tudelft.nl

ORCID

Ward van der Stam: 0000-0001-8155-5400

Notes

The authors declare no competing financial interest.

■ ACKNOWLEDGMENTS

A.J.H. acknowledges support from the European Research Council Horizon 2020 ERC Grant Agreement No. 678004 (Doping on Demand). Ben Norder is acknowledged for technical assistance during XRD measurements, Alma Olivos-Suarez and Jara Garcia Santaclara for assistance during Raman measurements, Bart Boshuizen for technical assistance during XPS measurements and Ryan Crisp for supplying the PbS NCs used for the PLQY measurements.

■ REFERENCES

(1) Roy, P.; Srivastava, S. K. *CrystEngComm* **2015**, *17*, 7801−7815.

(2) van der Stam, W.; Berends, A. C.; de Mello Donegá, C. *ChemPhysChem* **2016**, *17*, 559−581.

(3) Chakrabarti, D. J.; Laughlin, D. E. *Bull. Alloy Phase Diagrams* **1983**, *4*, 254−271.

(4) Willhammar, T.; Sentosun, K.; Mourdikoudis, S.; Goris, B.; Kurttepeli, M.; Bercx, M.; Lamoen, D.; Partoens, B.; Pastoriza-Santos, I.; Perez-Juste, J.; Liz-Marzan, L. M.; Bals, S.; Van Tendeloo, G. *Nat. Commun.* **2017**, *8*, 14925−14932.

(5) Wang, F.; Li, Q.; Lin, L.; Peng, H.; Liu, Z.; Xu, D. *J. Am. Chem. Soc.* **2015**, *137*, 12006−12012.

(6) Luther, J. M.; Jain, P. K.; Ewers, T.; Alivisatos, A. P. *Nat. Mater.* **2011**, *10*, 361−366.

(7) Posfai, M.; Buseck, P. *Am. Mineral.* **1994**, *79*, 308−315.

(8) Zhao, Y.; Pan, H.; Lou, Y.; Qiu, X.; Zhu, J.; Burda, C. *J. Am. Chem. Soc.* **2009**, *131*, 4253−4261.

(9) van der Stam, W.; Akkerman, Q. A.; Ke, X.; van Huis, M. A.; Bals, S.; de Mello Donega, C. *Chem. Mater.* **2015**, *27*, 283−291.

(10) Marbella, L. E.; Gan, X. Y.; Kaseman, D. C.; Millstone, J. E. *Nano Lett.* **2017**, *17*, 2414−2419.

(11) Xie, Y.; Carbone, L.; Nobile, C.; Grillo, V.; D'Agostino, S.; Della Sala, F.; Giannini, C.; Altamura, D.; Oelsner, C.; Kryschi, C.; Cozzoli, P. D. *ACS Nano* **2013**, *7*, 7352−7369.

(12) van der Stam, W.; Gradmann, S.; Altantzis, T.; Ke, X.; Baldus, M.; Bals, S.; De Mello Donega, C. *Chem. Mater.* **2016**, *28*, 6705−6715.

(13) Li, W.; Shavel, A.; Guzman, R.; Rubio-Garcia, J.; Flox, C.; Fan, J.; Cadavid, D.; Ibanez, M.; Arbiol, J.; Morante, J. R.; Cabot, A. *Chem. Commun.* **2011**, *47*, 10332−10334.

(14) Xie, Y.; Bertoni, G.; Riedinger, A.; Sathya, A.; Prato, M.; Marras, S.; Tu, R.; Pellegrino, T.; Manna, L. *Chem. Mater.* **2015**, *27*, 7531−7537.

(15) Dorfs, D.; Härtling, T.; Miszta, K.; Bigall, N. C.; Kim, M. R.; Genovese, A.; Falqui, A.; Povia, M.; Manna, L. *J. Am. Chem. Soc.* **2011**, *133*, 11175−11180.

(16) Kriegel, I.; Jiang, C.; Rodriguez-Fernandez, J.; Schaller, R. D.; Talapin, D. V.; Da Como, E.; Feldmann, J. *J. Am. Chem. Soc.* **2012**, *134*, 1583−1590.

(17) Kriegel, I.; Scotognella, F.; Manna, L. *Phys. Rep.* **2017**, *674*, 1−52.

(18) Xie, Y.; Riedinger, A.; Prato, M.; Casu, A.; Genovese, A.; Guardia, P.; Sottini, S.; Sangregorio, C.; Miszta, K.; Ghosh, S.; Pellegrino, T.; Manna, L. *J. Am. Chem. Soc.* **2013**, *135*, 17630−17637.

(19) Asami, K.; Nishi, H.; Tatsuma, T. *Nanoscale* **2016**, *8*, 14092−14096.

(20) Benavente Llorente, V.; Dzhagan, V. M.; Gaponik, N.; Iglesias, R. A.; Zahn, D. R. T.; Lesnyak, V. *J. Phys. Chem. C* **2017**, *121*, 18244−18253.

(21) Boehme, S. C.; Wang, H.; Siebbeles, L. D. A.; Vanmaekelbergh, D.; Houtepen, A. J. *ACS Nano* **2013**, *7*, 2500−2508.

(22) Ruch, P. W.; Cericola, D.; Hahn, M.; Kötz, R.; Wokaun, A. *J. Electroanal. Chem.* **2009**, *636*, 128−131.

(23) Hsu, S.-W.; Ngo, C.; Tao, A. R. *Nano Lett.* **2014**, *14*, 2372−2380.

(24) Liu, Y.; Liu, M.; Yin, D.; Wei, W.; Prasad, P. N.; Swihart, M. T. *Chem. Mater.* **2017**, *29*, 3555−3562.

(25) Liang, W.; Whangbo, M.-H. *Solid State Commun.* **1993**, *85*, 405−408.

(26) Goble, R. J. *Can. Mineral.* **1985**, *23*, 61−67.

(27) Lukashev, P.; Lambrecht, W. R. L.; Kotani, T.; van Schilfgaarde, M. *Phys. Rev. B: Condens. Matter Mater. Phys.* **2007**, *76*, 195202.

(28) Page, M.; Niitsoo, O.; Itzhaik, Y.; Cahen, D.; Hodes, G. *Energy Environ. Sci.* **2009**, *2*, 220−223.

(29) Wu, Y.; Wadia, C.; Ma, W.; Sadtler, B.; Alivisatos, A. P. *Nano Lett.* **2008**, *8*, 2551−2555.

(30) Zhao, Y.; Burda, C. *Energy Environ. Sci.* **2012**, *5*, 5564−5576.

(31) Neville, R. C. *Solar Energy Conversion: The Solar Cell*; Elsevier: Atlanta, GA, 1995.

(32) Boehme, S. C.; Vanmaekelbergh, D.; Evers, W. H.; Siebbeles, L. D. A.; Houtepen, A. J. *J. Phys. Chem. C* **2016**, *120*, 5164−5173.

(33) Tsui, E. Y.; Carroll, G. M.; Miller, B.; Marchioro, A.; Gamelin, D. R. *Chem. Mater.* **2017**, *29*, 3754−3762.

(34) Jiang, Q.; Chen, M.; Li, J.; Wang, M.; Zeng, X.; Besara, T.; Lu, J.; Xin, Y.; Shan, X.; Pan, B.; Wang, C.; Lin, S.; Siegrist, T.; Xiao, Q.; Yu, Z. *ACS Nano* **2017**, *11*, 1073−1079.

(35) Puntambekar, A.; Wang, Q.; Miller, L.; Smieszek, N.; Chakrapani, V. *ACS Nano* **2016**, *10*, 10988−10999.

(36) van de Krol, R. *J. Electrochem. Soc.* **1999**, *146*, 3150.

(37) Dahlman, C. J.; Tan, Y.; Marcus, M. A.; Milliron, D. J. *J. Am. Chem. Soc.* **2015**, *137*, 9160−9166.

(38) Jache, B.; Mogwitz, B.; Klein, F.; Adelhelm, P. *J. Power Sources* **2014**, *247*, 703−711.

(39) Justin Raj, C.; Kim, B. C.; Cho, W. J.; Lee, W. G.; Seo, Y.; Yu, K. H. *J. Alloys Compd.* **2014**, *586*, 191−196.

(40) Collinson, M. M. *ISRN Anal. Chem.* **2013**, *2013*, 692484.

(41) Henstridge, M. C.; Dickinson, E. J. F.; Compton, R. G. *Russ. J. Electrochem.* **2012**, *48*, 629−635.

(42) Bard, A. J.; Faulkner, L. R. *Electrochemical Methods: Fundamentals and Applications*, 2nd ed.; John Wiley & Sons, Inc.: Hoboken, NJ, 2001.

(43) Etienne, A. *J. Electrochem. Soc.* **1970**, *117*, 870−874.

(44) Cassaignon, S.; Pauporté, T.; Guillemoles, J.-F.; Vedel, J. *Ionics* **1998**, *4*, 364−371.

(45) Wang, X.; Liu, X.; Yin, D.; Ke, Y.; Swihart, M. T. *Chem. Mater.* **2015**, *27*, 3378−3388.

(46) van der Stam, W.; Berends, A. C.; Rabouw, F. T.; Willhammar, T.; Ke, X.; Meeldijk, J. D.; Bals, S.; de Mello Donega, C. *Chem. Mater.* **2015**, *27*, 621−628.
(47) Wang, X.; Swihart, M. T. *Chem. Mater.* **2015**, *27*, 1786−1791.
(48) Liu, Y.; Liu, M.; Swihart, M. T. *Chem. Mater.* **2017**, *29*, 4783−4791.
(49) Coughlan, C.; Ibáñez, M.; Dobrozhan, O.; Singh, A.; Cabot, A.; Ryan, K. M. *Chem. Rev.* **2017**, *117*, 5865−6109.
(50) Sands, T. D.; Washburn, J.; Gronsky, R. *Phys. Status Solidi* **1982**, *72*, 551−559.
(51) Lotfipour, M.; Machani, T.; Rossi, D. P.; Plass, K. E. *Chem. Mater.* **2011**, *23*, 3032−3038.
(52) Wang, Y.; Kim, J.; Gao, Z.; Zandi, O.; Heo, S.; Banerjee, P.; Milliron, D. J. *Chem. Mater.* **2016**, *28*, 7198−7202.
(53) Kim, J.; Ong, G. K.; Wang, Y.; LeBlanc, G.; Williams, T. E.; Mattox, T. M.; Helms, B. A.; Milliron, D. J. *Nano Lett.* **2015**, *15*, 5574−5579.
(54) Wang, Y.; Runnerstrom, E. L.; Milliron, D. J. *Annu. Rev. Chem. Biomol. Eng.* **2016**, *7*, 283−304.

DOI: 10.1021/jacs.7b07788
J. Am. Chem. Soc. 2017, 139, 13208−13217